Axisymmetric instabilities of Bödewadt flow

R. Fernandez-Feria[a)]
Universidad de Malaga, E. T. S. Ingenieros Industriales, 29013 Malaga, Spain

(Received 21 December 1999; accepted 3 April 2000)

A spatial linear stability analysis of Bödewadt's self-similar solution for the rotating flow over a flat plate is performed. In particular, considered is the stability of axisymmetric perturbations propagating towards the axis of rotation, which are the most important ones observed experimentally. Viscous and nonparallel effects on the stability of the perturbations are retained up to the order of the inverse of the local Reynolds number R. The resulting parabolic stability equations are solved numerically using a spectral collocation method varying the nondimensional frequency q and R. The instability region on the (q,R)-plane is discussed and compared with existing experimental data and direct numerical simulation results. The circular waves observed experimentally and in numerical simulations are shown to correspond to an inertial instability mode which becomes stabilized as R decreases below a critical value. © *2000 American Institute of Physics.* [S1070-6631(00)01307-6]

I. INTRODUCTION

The study of rotating flows over solid planes has been considered extensively in the literature because of both theoretical and technological interest. Of particular significance is the early work of Bödewadt,[1] who considered the flow produced over an infinite stationary plane in an incompressible fluid rotating with uniform angular velocity at an infinite distance from the plane. Bödewadt's flow constitutes an outstanding example of an analytical (self-similar) solution to the Navier–Stokes equations (see Sec. II A), analogous to that found earlier by von Kármán,[2] and generalized later by Batchelor.[3] Bödewadt's self-similar solution has been the subject of controversy[4] and, probably due to the experimental difficulties in creating a fluid in solid-body rotation over a stationary disk, only recently has been studied both experimentally and numerically.[5–8] In these works, quasisteady flows whose velocity profiles can be approximated to a high degree by Bödewadt's solution were originated in the interior of cylinders of several aspect ratios at different Reynolds numbers. Various types of instabilities propagating radially inwards on the stationary disk were described. Notably, axisymmetric (circular) waves travelling towards the center of the disk were found. The conjecture was made that these axisymmetric waves, which become stabilized below a critical local Reynolds number before reaching the center of the disk, represent a mode of instability of the Bödewadt flow. However, no detailed stability analysis of Bödewadt's solution is available to compare with these experimental and numerical results. The recent work by Lingwood[9] contains some scarce results on the stability of Bödewadt solution within a more general analysis of the absolute instability of a family of self-similar solutions for the Ekman layer, which includes Bödewadt's flow as a particular case. This author uses a parallel-flow approximation and finds that Bödewadt's flow is absolutely unstable above a critical Reynolds number which agrees well with the experimental values. In the present work, a nonparallel-flow approximation in the radial direction r is used to study the spatial stability of Bödewadt's solution, identifying a particular axisymmetric unstable mode as the one observed in the experiments and in the numerical simulations. Although the thickness of Bödewadt's self-similar layer is independent of r, nonparallel effects, that is the radial variation of the basic flow and of the amplitude of the perturbations, have to be considered in the stability equations at the same level as the viscous effects.

II. FORMULATION OF THE PROBLEM

A. Basic flow

Bödewadt's flow[1,10] is a self-similar solution to the Navier–Stokes equations for the stationary viscous flow over an infinite flat plate of an incompressible fluid rotating as a rigid body far from the plate. If Ω is the angular velocity of the rotating fluid over the plane, the viscous layer thickness is of the order of

$$\delta \equiv \sqrt{\nu/\Omega}, \tag{1}$$

where ν is the fluid kinematic viscosity. Bödewadt found that, in cylindrical polar coordinates (r,θ,z), where z is the axial coordinate perpendicular to the plate, with $r=0$ the axis of the rotating flow, the velocity field (U,V,W) on the plate can be written as

$$U=r\Omega f(\zeta), \quad V=r\Omega g(\zeta), \quad W=\sqrt{\nu\Omega}\, h(\zeta), \tag{2}$$

where

$$\zeta \equiv \frac{z}{\delta} = z\sqrt{\frac{\Omega}{\nu}}, \tag{3}$$

[a)]Electronic mail: ramon.fernandez@uma.es

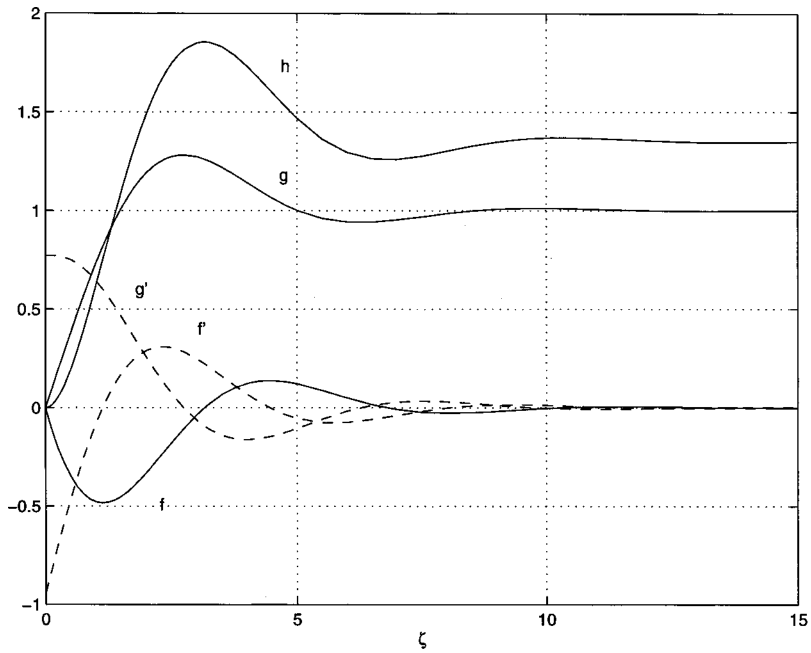

FIG. 1. Functions $f(\zeta)$, $g(\zeta)$, $h(\zeta)$, $f'(\zeta)$, and $g'(\zeta)$.

is the self-similar variable, and the functions (f,g,h) satisfy the following set of ordinary differential equations and boundary conditions (primes denote differentiation):

$$2f+h'=0, \tag{4}$$

$$f^2+hf'-g^2+1-f''=0, \tag{5}$$

$$2fg+hg'-g''=0, \tag{6}$$

$$f(0)=g(0)=h(0)=0, \quad f(\infty)=0, \quad g(\infty)=1. \tag{7}$$

Equations (4)–(6) come from the equations of continuity, r-momentum, and θ-momentum, respectively. The z-momentum equation determines the pressure field, except for an arbitrary constant, as

$$\frac{P}{\rho}=\frac{1}{2}r^2\Omega^2\left[1+2R^{-2}\left(h'-\frac{1}{2}h^2\right)\right], \tag{8}$$

where ρ is the fluid density, and R is the local Reynolds number, defined as

$$R\equiv\frac{r}{\delta}, \tag{9}$$

which will be assumed large. Figure 1 shows the profiles of f, g, h, f', and g', which have been obtained using a standard finite difference method with deferred corrections to solve the nonlinear problem (4)–(7).

B. Nonparallel linear stability formulation

To analyze the linear stability of the above basic flow, the flow variables (u,v,w) and p, are decomposed, as usual, into their mean parts (U,V,W) and P, and small perturbations. Following (2) and (8),

$$u=r\Omega[f(\zeta)+\overline{u}], \tag{10}$$

$$v=r\Omega[g(\zeta)+\overline{v}], \tag{11}$$

$$w=r\Omega[R^{-1}h(\zeta)+\overline{w}], \tag{12}$$

$$\frac{p}{\rho}=\frac{1}{2}r^2\Omega^2[1+\overline{p}], \tag{13}$$

where the perturbations

$$\mathbf{s}\equiv[\overline{u},\overline{v},\overline{w},\overline{p}]^T \tag{14}$$

are in general functions of the four independent variables (r,θ,z,t). Note that the term $O(R^{-2})$ in the basic pressure field (8) has been neglected, which is consistent with the stability analysis given below. Since the mean flow depends on the similarity variable ζ, this nondimensional variable is used instead of z. Also, as nondimensional radial coordinate we use the local Reynolds number (9). The perturbations (14) are decomposed in the standard form:

$$\mathbf{s}(R,\zeta,\theta,t)=\mathbf{S}(R,\zeta)\chi(R,\theta,t), \tag{15}$$

where the complex amplitude

$$\mathbf{S}(R,\zeta)\equiv\begin{pmatrix} F(R,\zeta)\\ G(R,\zeta)\\ H(R,\zeta)\\ \Pi(R,\zeta)\end{pmatrix} \tag{16}$$

depend on both the radial and the axial coordinates. The other part of the perturbation is of exponential form that describes the wavelike nature of the disturbance,

$$\chi(R,\theta,t)=\exp\left[\int_{R_i}^{R}a(R')dR'+i(n\theta-\omega t)\right], \tag{17}$$

where R_i is an initial or reference Reynolds number. The nondimensional, order of unity, complex radial wave number a is defined, in terms of its dimensional value k, as

$$a(R)\equiv\delta k(R)\equiv\gamma(R)+i\alpha(R). \tag{18}$$

The real part $\gamma(R)$ is the local exponential growth rate, and the imaginary part $\alpha(R)$ is the local radial wave number. A nondimensional frequency q is also defined

$$q \equiv \frac{\omega}{\Omega}. \tag{19}$$

Finally, the azimuthal wave number n is equal to zero for axisymmetric perturbations, and different from zero for spiral perturbations.

Substituting (15)–(19) into the incompressible Navier–Stokes equations, and neglecting second-order terms in both the small perturbations and R^{-1}, the following set of linear parabolic stability equations results:

$$\mathbf{L}\cdot\mathbf{S}+\mathbf{M}\cdot\frac{\partial\mathbf{S}}{\partial R}=\mathbf{0}, \tag{20}$$

where the matrix operators $\mathbf{L}$ and $\mathbf{M}$ are defined as

$$\mathbf{L}\equiv\mathbf{L}_1+a\mathbf{L}_2+\frac{1}{R}\mathbf{L}_3-a^2\frac{1}{R}\mathbf{L}_4, \tag{21}$$

$$\mathbf{L}_1=\begin{pmatrix} 0 & 0 & \partial/\partial\zeta & 0\\ 0 & 0 & f' & 0\\ 0 & 0 & g' & 0\\ 0 & 0 & 0 & \frac{1}{2}\partial/\partial\zeta \end{pmatrix}, \tag{22}$$

$$\mathbf{L}_2=\mathbf{M}=\begin{pmatrix} 1 & 0 & 0 & 0\\ f & 0 & 0 & 1/2\\ 0 & f & 0 & 0\\ 0 & 0 & f & 0 \end{pmatrix},\qquad \mathbf{L}_4=\begin{pmatrix} 0 & 0 & 0 & 0\\ 1 & 0 & 0 & 0\\ 0 & 1 & 0 & 0\\ 0 & 0 & 1 & 0 \end{pmatrix}, \tag{23}$$

$$\mathbf{L}_3=\begin{pmatrix} 2 & in & 0 & 0\\ -iq+2f+ing+D_\zeta & -2g & 0 & 1\\ 2g & -iq+2f+ing+D_\zeta & 0 & in/2\\ 0 & 0 & -iq+2f+ing+h'+D_\zeta & 0 \end{pmatrix}, \tag{24}$$

with

$$D_\zeta\equiv h\partial/\partial\zeta-\partial^2/\partial\zeta^2. \tag{25}$$

The above equations must be solved with the following boundary conditions at $\zeta=0$ and $\zeta\rightarrow\infty$:

$$\begin{aligned} &F(R,\infty)=G(R,\infty)=H(R,\infty)=0,\\ &F(R,0)=G(R,0)=H(R,0)=0. \end{aligned} \tag{26}$$

An initial condition at some large value of R is also needed to solve (20). However, this last condition will not be used here because we shall look for local solutions (but retaining $\partial/\partial R$ terms) of the parabolized stability equations (see next section).

In the above approximation, terms $O(R^{-2})$ and smaller have been neglected. The retained $O(R^{-1})$ terms account for three different effects on the stability of the perturbations: (i) the effect of viscosity, (ii) the effect of the nonparallelism of the basic flow and of the amplitude of the perturbations, and (iii) the effect of the history, or convective evolution, of the perturbations. This last effect (iii) is described by the $\partial/\partial R$ terms of the stability equations, which are the ones responsible for the partial differential (though parabolic) character of the equations. All three effects are therefore negligible in the limit $R\rightarrow\infty$. Note that both the nondimensional frequency q and the azimuthal wave number n enter into the equations at order R^{-1} (operator $\mathbf{L}_3$). Therefore, the significant frequency values ω of the perturbations should be large in relation to Ω (q/R cannot be very small for large R), and the stability results for $n\neq 0$, $|n|=O(1)$, should not differ much from the results for $n=0$. For this last reason, and because experimental observations show that the most interesting instability waves of Bödewadt flow are axisymmetric ones (e.g., Savaş,[6] and Gauthier *et al.*[8]), only the case $n=0$ will be considered in this work.

C. Stability definitions and numerical method

As it stands there is some ambiguity in the partition of the perturbations (15) into two functions of the radial coordinate R. To close the problem one has to enforce an additional normalization condition which puts some restriction on the radial variation of the perturbation eigenfunction.[11] We shall perform here a local spatial stability analysis: Given a *real* frequency q and the azimuthal wave number n, Eq. (20) and its R derivative will be solved locally for each radius $R=R_0$ with the *normalization* condition $[\partial a/\partial R]_{R=R_0}=0$. This condition will restrict, as required, the downstream variation of the perturbation eigenfunction, yielding, for each R, the local growth rate and radial wave number (or the phase speed of the disturbance) as functions of the axial distance to the plate ζ.

The eigenfunction $\mathbf{S}$ is expanded in a Taylor series about

$R=R_0$, where only two terms are retained to be consistent with the approximations made in the preceding section:

$$\mathbf{S}(R,\zeta)\simeq\mathbf{S}(R_0,\zeta)+(R-R_0)\left.\frac{\partial\mathbf{S}(R,\zeta)}{\partial R}\right|_{R=R_0}$$
$$\equiv\mathbf{S}_0(\zeta)+(R-R_0)\mathbf{S}_1(\zeta). \tag{27}$$

This expansion is now substituted into (20) and its R derivative to obtain two equations for $\mathbf{S}_0$ and $\mathbf{S}_1$ ($|\mathbf{S}_1|\ll|\mathbf{S}_0|$). Using the local normalization condition $[\partial a(R)/\partial R]_{R=R_0}=0$, one has

$$\mathbf{L}\cdot\mathbf{S}_0+\mathbf{M}\cdot\mathbf{S}_1=\mathbf{0}, \tag{28}$$

$$\frac{iq}{R^2}\mathbf{L}_4\cdot\mathbf{S}_0+\mathbf{L}'\cdot\mathbf{S}_1=\mathbf{0}, \tag{29}$$

where the operator $\mathbf{L}$ is now evaluated at $R=R_0$ and $\mathbf{L}'=\mathbf{L}_1+a\mathbf{L}_2-iq\mathbf{L}_4/R$. Note that terms $O(q/R^2)$ have been retained to allow for high values of the frequency q. For given q, n, and $R=R_0$, this constitutes a nonlinear eigenvalue problem for the complex eigenvalue a and the complex eigenfunction

$$\mathbf{X}(\zeta)\equiv\begin{pmatrix}\mathbf{S}_0\\ \mathbf{S}_1\end{pmatrix}. \tag{30}$$

Experimental and numerical results[6–8] show that the instability waves propagate towards the axis, i.e., in the same direction as the bulk of the radial flow (see Fig. 1). Thus, for a given positive value of q, one is interested in modes whose eigenvalue a has both its real and imaginary parts negative. According to (17) and (18), this ensures that the perturbation grows exponentially as it propagates towards decreasing R ($\gamma<0$), with phase velocity directed towards the axis (i.e., $\alpha<0$). We are mostly interested in the evolution as R decreases of the most unstable mode (largest $|\gamma|$) for given values of q and $n=0$, and in how this evolution depends on the distance ζ to the plate. To that end we define a nondimensional *physical* growth rate γ_u, and a nondimensional *physical* radial wave number α_u, based on the radial velocity component of the perturbation $(r\Omega\overline{u})$:

$$a_u\equiv-\frac{\delta}{r\Omega\overline{u}}\frac{\partial}{\partial r}(r\Omega\overline{u}), \tag{31}$$

$$\gamma_u(R,\zeta)\equiv\Re(a_u)=-\gamma(R)-\frac{1}{R}-\Re\left(\frac{F_1(\zeta)}{F_0(\zeta)}\right), \tag{32}$$

$$\alpha_u(R,\zeta)\equiv\Im(a_u)=-\alpha(R)-\Im\left(\frac{F_1(\zeta)}{F_0(\zeta)}\right), \tag{33}$$

where $F_0(\zeta)=F(R_0,\zeta)$ and $F_1(\zeta)=[\partial F(R,\zeta)/\partial R]_{R=R_0}$ (for simplicity, in the above expressions and in what follows we write R for R_0). The nondimensional local phase speed of the disturbances is defined in terms of α_u:

$$c_u(R,\zeta)\equiv\frac{q}{R\,\alpha_u(R,\zeta)} \tag{34}$$

(note that the dimensional local phase speed is Ωr times c_u). Finally, to measure the global growth rate of the disturbances, it is convenient to define an integral growth rate,

$$\gamma^I(R)=\frac{\int_0^\infty\gamma_u(R,\zeta)|F(R,\zeta)|d\zeta}{\int_0^\infty|F(R,\zeta)|d\zeta}, \tag{35}$$

which is more appropriate than the real part of the eigenvalue, $-\gamma$, to characterize the amplification rate of the perturbations.

To solve (28)–(29) numerically, the ζ-dependence of $\mathbf{X}$ is discretized using a staggered Chebyshev spectral collocation technique developed by Khorrami.[12] This method has the advantage of eliminating the need of two artificial pressure boundary conditions at $\zeta=0$ and $\zeta=\infty$, which are not included in (26). The boundary conditions at infinity are applied at a truncated radial distance $\zeta_{\max}$, chosen large enough to ensure that the results do not depend on that truncated distance (values of $\zeta_{\max}$ between 20 and 140 were used in the computations reported below). To implement the spectral numerical method, Eqs. (28) and (29) are discretized by expanding $\mathbf{X}$ in terms of truncated Chebyshev series. A nonuniform coordinate transformation is used to map the interval $0\leqslant\zeta\leqslant\zeta_{\max}$ into the Chebyshev polynomial domain $-1\leqslant s\leqslant1$: $\zeta=c_1-c_2\ln(1+\epsilon-s)$, where $c_1=c_2\ln(2+\epsilon)$, $c_2=\zeta_{\max}/(\ln(2+\epsilon)-\ln\epsilon)$ and ϵ is a very small number ($\epsilon=10^{-3}$ is used). This transformation allows large values of ζ to be taken into account with relatively few basis functions.

The ζ domain is thus discretized in N points, N being the number of Chebyshev polynomials in which $\mathbf{X}$ has been expanded. In the results presented here, N ranged between 40 and 165. With this discretizazion, (28) and (29) become an algebraic nonlinear eigenvalue problem which is solved using the linear companion matrix method described by Bridges and Morris.[13] The resulting (complex) linear eigenvalue problem is solved with double precision using an eigenvalue solver from the IMSL library, which provides the entire eigenvalue and eigenvector spectrum. Since the dimension of the associated linear problem is $16N$, the computation time increases very fast with the number of nodal points N. Also, due to the large dimension of the matrices, a relatively large amount of spurious numerical eigenvalues are produced by the eigenvalue solver, particularly when q is very small. They are, however, easily discarded because the corresponding growth rates change wildly as N increases, instead of rapidly converging to a finite value, as happens for eigenvalues of the physical modes.

III. RESULTS AND DISCUSSION

A. Inviscid and parallel results

In order to gain a preliminary insight on the stability properties of Bödewadt's flow, it is convenient to analyze the inviscid and parallel solutions of the stability problem; that is to say, the limit $R\to\infty$. Neglecting terms $O(R^{-1})$ in (20), one has

$$(\mathbf{L}_1+a\mathbf{L}_2-iq^*\mathbf{L}_4)\cdot\mathbf{S}=\mathbf{0}, \tag{36}$$

where

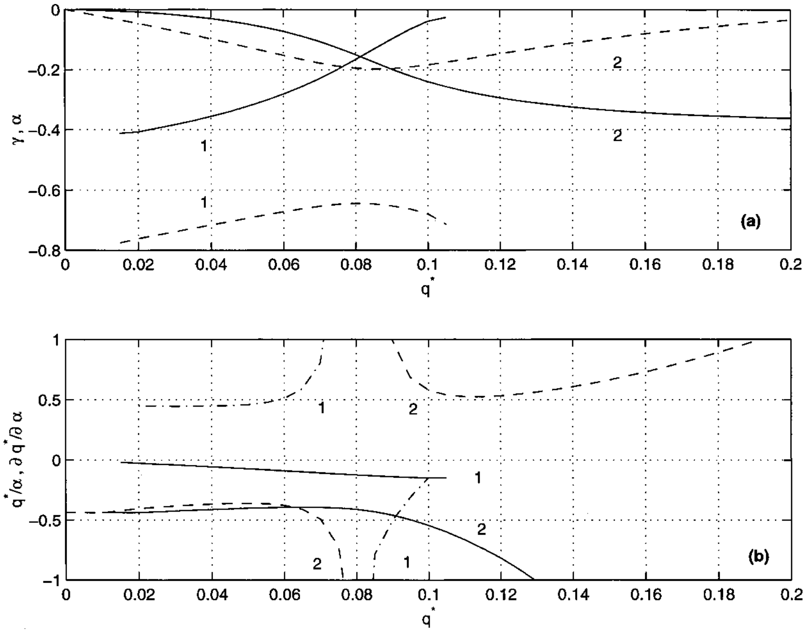

FIG. 2. (a) Real (γ, continuous lines) and imaginary (α, dashed lines) parts of the eigenvalue a for the two most unstable modes (1 and 2) propagating towards the axis when $R \to \infty$ as functions of the local frequency q^*. They are numerically obtained with $N=300$ and values of $\zeta_{\max}$ between 20 and 200. (b) Local phase velocity q^*/α (continuous lines) and local group velocity (dashed and dashed–dotted lines) of modes 1 and 2 as functions of q^* for $R \to \infty$.

$$q^* = \frac{q}{R}, \tag{37}$$

is the *local* frequency. The term proportional to q/R has been retained because one is interested in how the spatial stability properties change with the frequency. In addition, as we shall see, there is no eigenvalue $a \neq 0$ satisfying the above equation for $q^*=0$, so that the term has to be retained. The azimuthal wave number n does not appear in this limit $R \to \infty$. Equation (36) can be reduced to a single scalar equation for the axial component H of $\mathbf{S}$:

$$H'' + H\left(a^2 - \frac{af''}{af - iq^*}\right) = 0, \tag{38}$$

where the primes denote differentiation with respect to ζ (note that the eigenfunctions are now independent of R, except implicitly through q^*). This Rayleigh-type equation has to be solved with the boundary conditions

$$H(0) = H(\infty) = 0. \tag{39}$$

The remaining eigenfunctions are related to H through

$$F = -\frac{H'}{a}, \quad G = \frac{g'H}{iq^* - af}, \quad \Pi' = 2H(iq^* - af). \tag{40}$$

For real frequency q^*, Eqs. (38) and (39) constitute a cubic eigenvalue problem for the complex eigenvalue a and the complex eigenfunction H. For $q^*=0$, the problem has no

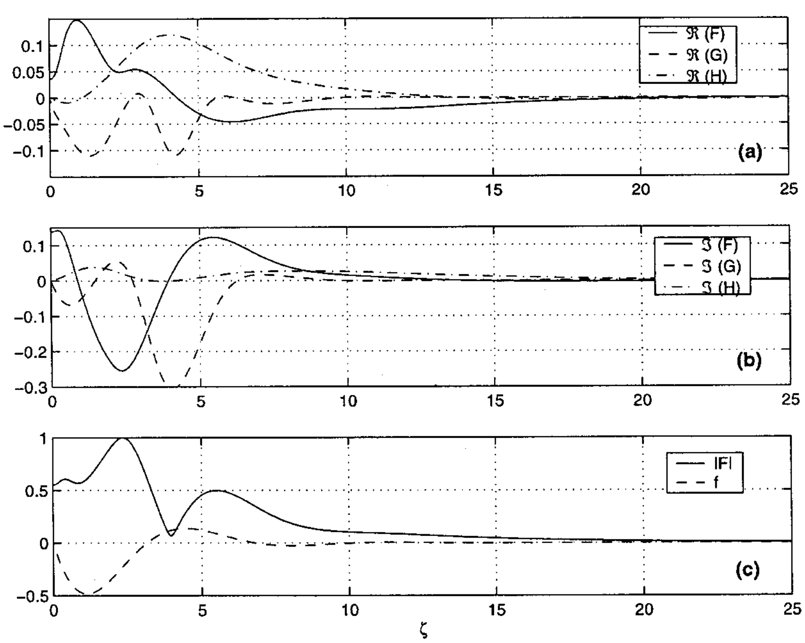

FIG. 3. Real (a) and imaginary (b) parts of the eigenfunctions $F(\zeta)$, $G(\zeta)$, and $H(\zeta)$ corresponding to mode 2 in the limit $R \to \infty$ for the most unstable frequency $q^* = q_0^* \simeq 0.081$. (c) $|F(\zeta)|$ compared to the radial velocity profile $f(\zeta)$. The maximum of $|F(\zeta)|$ is normalized to unity.

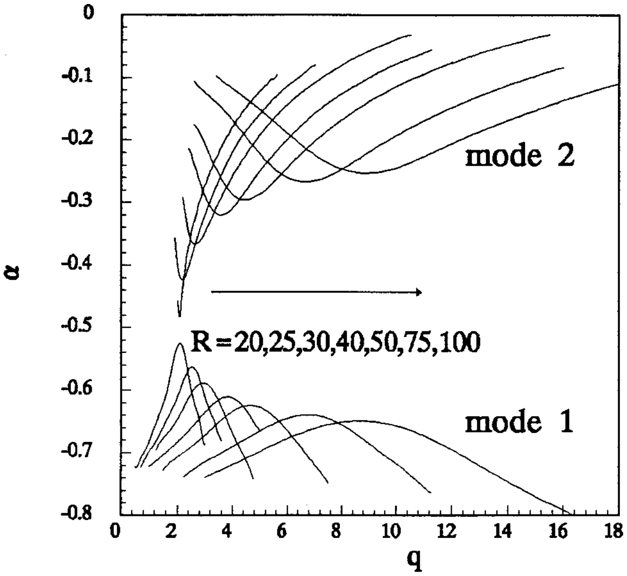

FIG. 4. Dispersion relations $\alpha(q)$ of modes 1 and 2 for several Reynolds numbers.

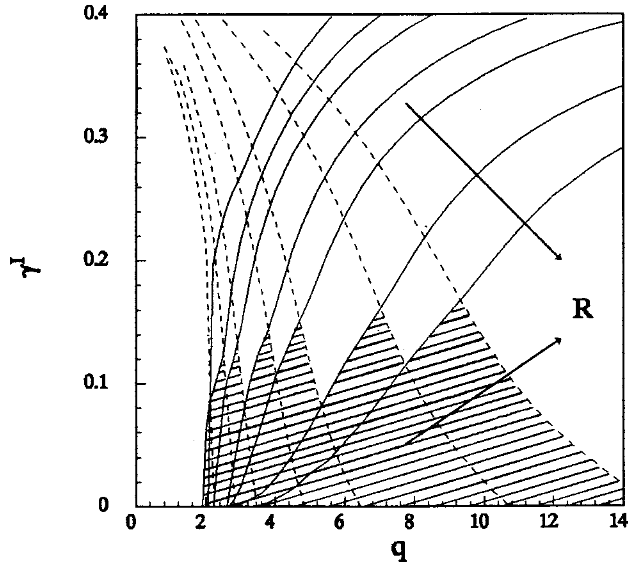

FIG. 5. Integral growth rates $\gamma^I(q)$ of modes 1 (dashed lines) and 2 (continuous lines) for the same Reynolds numbers of Fig. 4.

solution, except for the trivial one $a=0$. For each $q^*>0$, if H is an eigenfuction with eigenvalue a, then so too is $-H^\dagger$ with eigenvalue $-a^\dagger$, where † denotes the complex conjugate, for the same q^*. Thus, to each mode with growth rate γ and wave number α there is a corresponding mode with growth rate $-\gamma$ and the same α, i.e., the same phase velocity. If $\alpha<0$, the wave propagates towards the axis (decreasing R), so that the mode with $\gamma<0$ is unstable, while the corresponding mode with $\gamma>0$ is stable. Conversely, for $\alpha>0$, the mode with $\gamma>0$ is unstable and its counterpart with $\gamma<0$ is stable. As discussed in the preceding section, we shall look for unstable modes propagating towards the axis ($\alpha<0$ and $\gamma<0$).

The cubic eigenvalue problem (38) and (39) is numerically solved using the linear companion matrix method.[13] Previously, Eq. (38) is discretized in N nodes by a spectral collocation method, so that the associated linear eigenvalue problem has dimension $3N$. Figure 2(a) shows the real and imaginary parts of a as functions of q^* corresponding to the two most unstable modes (highest values of $|\gamma|$) propagating towards the axis, i.e., with negative values of both γ and α. The growth rates γ_1 and γ_2 of these two modes cross at $q=q_0^*\simeq 0.081$. It must be noted here that there exists a third unstable inviscid mode with higher values of $|\gamma|$ than modes 1 and 2 in part of the frequency range plotted in Fig. 2(a), but which is not considered here because it is associated to positive values of α and, therefore, to perturbations with phase velocity directed away from the axis.

The most interesting feature of Fig. 2(a) is that the slope of the dispersion relations $\alpha_1(q^*)$ and $\alpha_2(q^*)$ of the most unstable modes 1 and 2 change their sign, and therefore the direction of their group velocities, at the same frequency q_0^* (approximately) at which $\gamma_1=\gamma_2$. This can be better appreciated in Fig. 2(b), where the local phase velocity q^*/α, and the local group velocity $\partial q^*/\partial\alpha$, are plotted as functions of q^*. Although $|\gamma_1|>|\gamma_2|$ for $q^*<q_0^*$, mode 1 has a positive group velocity, that is in the opposite direction to the phase velocity of the perturbation. Hence, the most unstable *physical* mode for $q^*<q_0^*$ is mode 2, which in this frequency range has phase and group velocities with the same (negative) sign. Actually, both velocities almost coincide until $q^*\approx 0.06$. As q^* approaches q_0^*, the group velocity of mode 2 becomes singular, and then changes its sign for $q^*>q_0^*$ [dashed line in Fig. 2(b)], which clearly indicates that this mode is no longer physically meaningful for $q^*\geqslant q_0^*$. That mode 2 is the physically relevant one at low frequencies is also consistent with the fact that only mode 2 satisfies (38) in the limit $q^*\to 0$ [$\alpha_2(0)=\gamma_2(0)=0$], while mode 1 presents a discontinuity as $q^*\to 0$.

Conversely, although $|\gamma_2|>|\gamma_1|$ for $q^*>q_0^*$, mode 2 has a positive group velocity in this frequency range and must be physically discarded. This is corroborated by the fact that the growth rate γ_2 tends to a nonvanishing asymptote as the frequency increases, instead of going to zero like γ_1 [Fig. 2(a)]. Consequently, the most unstable perturbation propagating towards the axis is that associated to mode 2 for $q^*<q_0^*$, and the one associated to mode 1 for $q^*>q_0^*$. According to this, perturbations propagating towards the axis are inviscidly unstable in the range of local frequencies $0<q^*<0.12$, approximately, the most unstable frequency of which in this limit $R\to\infty$ is $q^*=q_0^*\simeq 0.081$. These frequencies are in the range of the smaller experimental values of Savaş[6] corresponding to the higher Reynolds numbers considered in his Fig. 8(b). On the other hand, Fig. 8(a) of Savaş[6] shows that the observed wave number for *large* Reynolds numbers ($R>100$, approximately; see also Fig. 7 below) is about 0.2, thus indicating that mode 2 is the one observed experimentally [note from Fig. 2(a) that the wave numbers of modes 1 and 2 at $q^*=q_0^*$ are $-\alpha_{01}\simeq 0.645$ and $-\alpha_{02}\simeq 0.198$, respectively]. The eigenfunctions corresponding to mode 2 at $q^*=q_0^*$ in the present limit $R\to\infty$ are shown in Fig. 3.

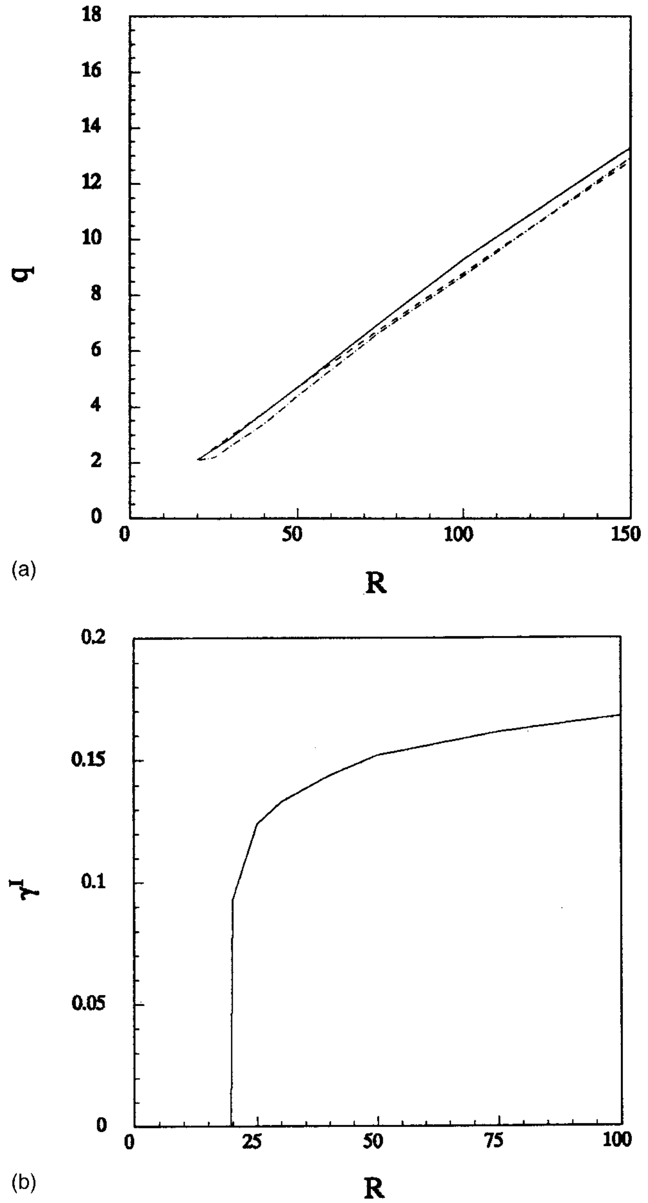

FIG. 6. (a) $q_0(R)$ (continuous line), $q_{01}(R)$ (dashed line), and $q_{02}(R)$ (dashed–dotted line). (b) γ_2^I for $q=q_0(R)$.

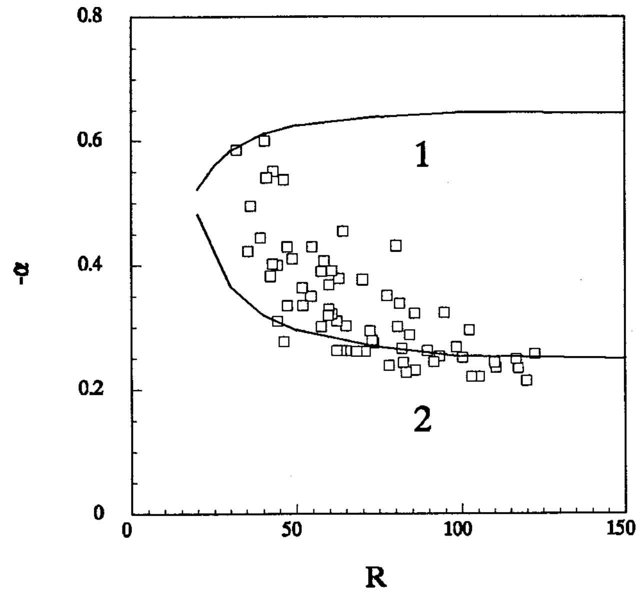

FIG. 7. Continuous lines: $-\alpha_{01}(R)$ and $-\alpha_{02}(R)$ at $q_{01}(R)$ and $q_{02}(R)$, respectively. □: experimental wave numbers reported by Savaş.[6]

B. Nonparallel and viscous results for $n=0$

In this section we present the results for finite, but large, Reynolds numbers R, thus accounting for the viscous and nonparallel effects on the stability of the perturbations. In particular, we shall give the results for the most unstable axisymmetric ($n=0$) perturbations propagating towards the axis, which, according to the results of the previous section, correspond to the inviscid mode 2 for low frequencies, and to the inviscid mode 1 for high frequencies. More precisely, mode 2 is the most unstable physical mode for $q<q_{02}(R)$, where $q_{02}(R)$ is the frequency at which the group velocity of mode 2 becomes singular and then changes its sign for each Reynolds number R [i.e., where $\alpha_2(q)$ has its minimum for each R]. Mode 1 is the most unstable for $q>q_{01}(R)$, being $q_{01}(R)$ the frequency at which $\alpha_1(q)$ has its maximum for each R. As it happened with the corresponding inviscid modes, these frequency values $q_{01}(R)$ and $q_{02}(R)$ almost coincide with each other and with the frequency $q_0(R)$ where the integral growth rates γ^I of modes 1 and 2 cross [note that in the limit $R\to\infty$, $\gamma_u(R,\zeta)$ does not depend on ζ, so that $\gamma^I=-\gamma$]. Figure 4 shows $\alpha_1(q)$ and $\alpha_2(q)$ for several values of R. It is observed that the maxima and the minima of these functions $\alpha(q)$ become sharper as R decreases. Figure 5 shows $\gamma_1^I(q)$ and $\gamma_2^I(q)$ for the same values of R. The shaded areas correspond to the *physical* values for which phase and group velocities have the same (negative) sign. The frequencies $q_0(R)$, $q_{01}(R)$, and $q_{02}(R)$ are plotted in Fig. 6(a). These frequencies are in the range of the experimental values reported by Savaş[6] (note that his Fig. 8(b) plots the local frequency $q^*=q/R$ instead of q). For $20<R<100$, $q_0(R)$ can be approximated by the linear function $q_0(R)\simeq 0.18+0.091R$. Figure 6(b) shows the maximum values of the integral growth rate γ^I [at $q=q_0(R)$, where $\gamma_1^I=\gamma_2^I$] as a function of R. The nondimensional radial wave numbers $\alpha_{01}(R)$ and $\alpha_{02}(R)$ of modes 1 and 2 at $q_{01}(R)$ and $q_{02}(R)$, respectively, are plotted in Fig. 7. As discussed above, they correspond, approximately, to the wave numbers of modes 1 and 2 at the frequencies where $\gamma_1^I=\gamma_2^I$. Also plotted in Fig. 7 are the experimental values reported by Savaş[6] [his Fig. 8(a)], which are in good agreement with $-\alpha_{02}$, indicating again that mode 2, which is the most unstable one at low frequencies, corresponds to the observed axisymmetric instabilities propagating towards the axis.

Finally, Fig. 8 summarizes some of the above results, showing the instability region in the (q,R) plane (it corresponds to the shaded areas in Fig. 5). The upper curve is the neutral instability curve for mode 1, while the lower one is the neutral curve for mode 2. The dashed line corresponds to the most unstable perturbations [$q=q_0(R)$, Fig. 6(a)], with corresponding growth rates plotted in Fig. 6(b). All these curves cross at the critical Reynolds number $R_c\simeq 19.8$ and frequency $q_c\simeq 2.1$, corresponding to a (mode 2) wave num-

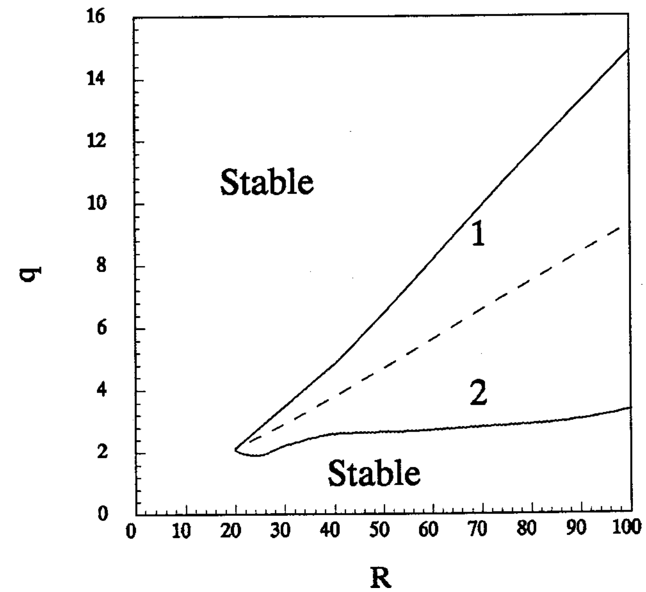

FIG. 8. Instability region in the (q,R) plane for axisymmetric perturbations. The dashed line corresponds to the most unstable perturbations $[q=q_0(R)]$.

ber $-\alpha_c \simeq 0.482$. Thus, Bödewadt's flow is stable for axisymmetric perturbations for Reynolds numbers below R_c. This critical Reynolds number is lower than the experimental result $R_c \approx 24.5$ of Savaş,[6] and the direct numerical simulation results of Lopez and Weidman[7] (R_c between 25 and 30). The discrepancies may be due, apart from numerical and experimental indeterminacies, to the finite aspect ratio of the cylinders used in the experiments and in the numerical simulations, in contrast to the infinite domain of the self-similar solution. This is corroborated by the fact that the experiments performed by Gauthier *et al.*[8] with a cylinder of much larger aspect ratio (ratio between the radius and the height of the cylinder equal to 20.9) yield a minimum Reynolds number as high as 140 for the observation of circular waves propagating radially inwards. On the other hand, the critical values of R_c and α_c found here are in good agreement with those obtained by Lingwood[9] for the onset of absolute instability.

As commented on in Sec. II C, the present method yields not only global or integral stability results, but also the variation of the stability properties of the perturbations across the boundary layer. Figures 9 and 10 show the physical growth rate γ_u and the physical wave number α_u of mode 2 as functions of ζ for two Reynolds numbers, $R=100$ and $R=30$, at their corresponding most unstable frequency $q_0(R)$. Also plotted is the absolute value of the radial eigenfunction, $|F(\zeta)|$, and the eigenvalues, $-\gamma$ and $-\alpha$. It is observed that the variation across the boundary layer of γ_u and α_u becomes more important as the local Reynolds number decreases, which otherwise is evident from their definitions (32) and (33). Consequently, larger values of both N and $\zeta_{\max}$ are needed to obtain numerically the eigenfunctions and eigenvalues as R decreases, increasing considerably the computation time and computer memory (as R approached R_c, $N=165$ was used, which is the highest number of ζ nodes that can reasonably be managed by our computer, a Silicon Graphics Origin 2000, using 512 Mb of shared RAM). On the other hand, the computed values of γ_u and α_u fail at the wall due to the fact that both F_1 and F_0 vanish at $\zeta=0$, appearing a singularity in (32) and (33). The singularity is more important as R decreases because of the increasing accuracy needed to obtain the eigenfunctions. The computed integral growth rates (and, of course, the eigenvalues) are not, however, affected by this singularity, converging very rapidly as N increases (they can be very accurately computed using values of N much lower than 165 even for R near R_c).

The physical growth rate $\gamma_u(\zeta)$ is smaller than the eigenvalue $-\gamma$ [Figs. 9(b) and 10(b)], except very close to the wall (where, as stated above, it is not very accurately computed) and other discrete locations where the amplitude $|F|$ of the perturbation is zero or has a local minimum. On the

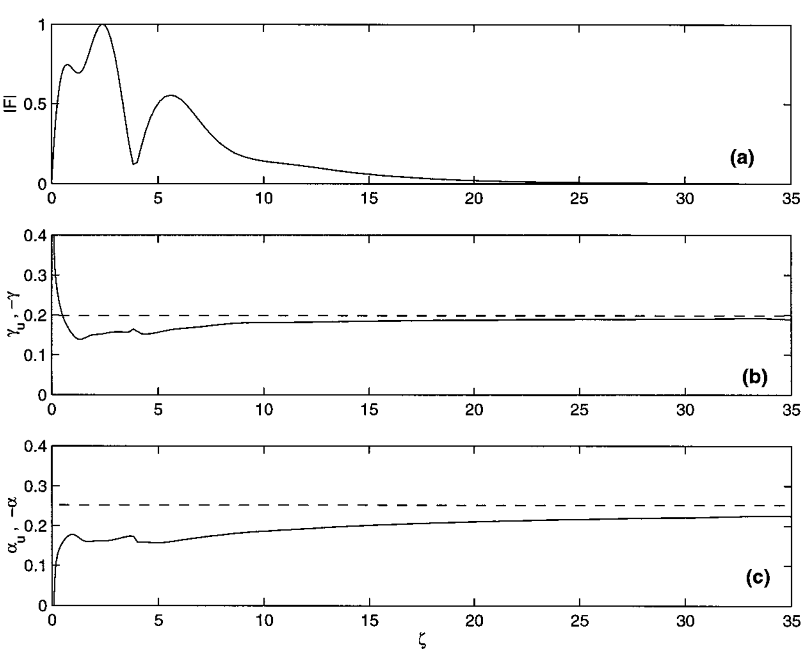

FIG. 9. Eigenfunction, physical growth rate, and wave number, as functions of ζ, for $R=100$ and $q=q_0(100)\simeq 9.3$ (mode 2). (a) $|F(\zeta)|$ with its maximum value normalized to unity. (b) $\gamma_u(\zeta)$; the dashed line corresponds to $-\gamma$. (c) $\alpha_u(\zeta)$; the dashed line corresponds to $-\alpha$. ($N=90$ and $\zeta_{\max}=40$.)

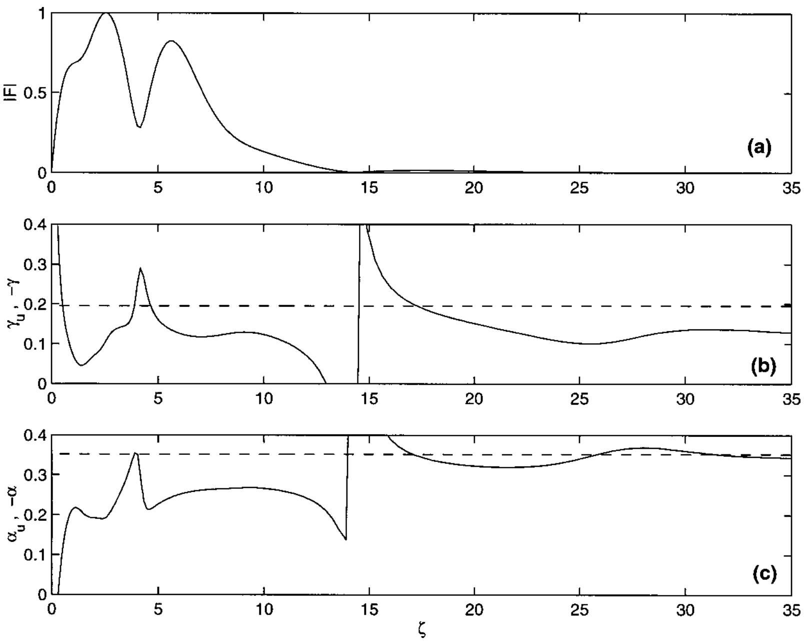

FIG. 10. As in Fig. 9 but for $R=30$ and $q=q_0(30) \simeq 2.9$. ($N=165$ and $\zeta_{\max}=80$.)

other hand, a local minimum of γ_u is located near the value of ζ where $|F|$ has a maximum. Consequently, the integral growth rate γ^I is always smaller than $-\gamma$. The wave number α_u is also smaller than $-\alpha$ for the most significant values of ζ where $|F|$ is not nearly zero [Figs. 9(c) and 10(c)]. This means that the local phase speed of the perturbations is larger, for most values of ζ, than that obtained using the imaginary part α of the eigenvalue. This is clear in Fig. 11, where the phase speed based on the eigenvalue α for $q=q_0(R)$ is compared to the phase speed c_u evaluated according to (34) at $\zeta=2.5$ (where the amplitude of the perturbation $|F|$ has its maximum, approximately, for all R) for disturbances corresponding to mode 2. These last values of the phase speed are in the range of the ones obtained by Lopez and Weidman[7] in their numerical simulations, which range between 0.2 and 0.55, approximately (note that to obtain the actual local phase speeds one has to multiply c_u by Ωr).

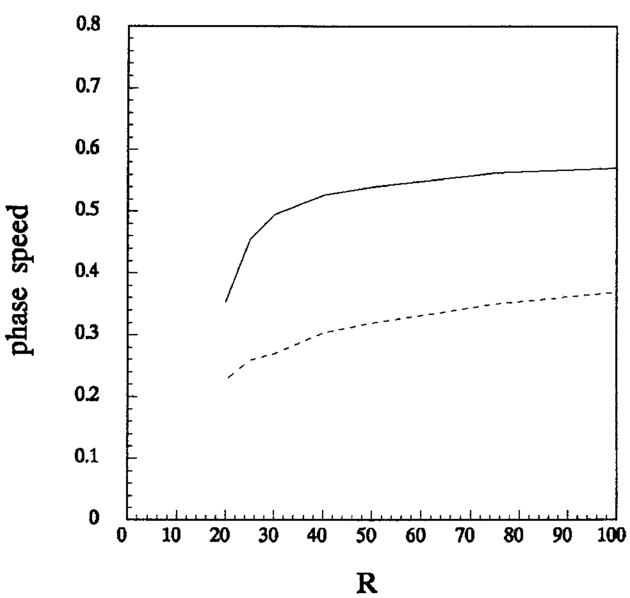

FIG. 11. Local phase speed of the perturbations c_u corresponding to mode 2 at $\zeta=2.5$ (continuous line) as function of R for $q=q_0(R)$. The dashed line represents the phase speed based on the eigenvalue α for the same values of q and R, i.e., $-q/[R\ \alpha_2(q_0)]$.

IV. CONCLUSIONS

A linear spatial stability analysis of Bödewadt's self-similar solution has shown that the circular waves observed experimentally, and in numerical simulations, in the boundary layer over the stationary endwall of a cylinder with a fluid in solid body rotation correspond to a particular instability mode of that self-similar solution (termed here as ''mode 2''). Since this unstable mode is present at infinite Reynolds numbers, it corresponds to an inertial instability. It is the most unstable one at low frequencies, up to the local frequency $q/R=q_0^* \simeq 0.081$, at which the local group velocity of the perturbations becomes unbounded, and then changes its sign for larger q/R. Thus, for $q/R>q_0^*$, the most unstable physical mode shifts from mode 2 to another one, termed here as ''mode 1,'' which is not observed in the experiments and in the numerical simulations. In this high Reynolds number limit, the most unstable frequency and wave number found here are $q/R \simeq 0.081$ and $|\alpha| \simeq 0.2$, respectively. As R decreases, viscous and nonparallel effects, which are $O(R^{-1})$, become increasingly more important in the stability properties of the flow, increasing slowly both the local frequency and the wave number of the most unstable perturbations. Eventually, the circular waves travelling radially inwards are stabilized by these effects, and no axisymmetric perturbation is unstable below a critical local Reynolds number $R_c \approx 20$, corresponding to $q_c \approx 2.1$ and $|\alpha_c| \approx 0.48$. The discrepancies between these critical values and the reported ones from experiments and numerical simulations are probably due to the finite height and radius of the cylinders where they are performed.

ACKNOWLEDGMENTS

This research has been supported by the DGES of Spain (Grant No. PB96-0679-C02-01). I have benefitted from comments by Professor John Lopez. Acknowledgment is also due to Professor O. Savaş for providing his experimental data plotted in Fig. 7.

[1] U. Bödewadt, Z. Angew. Math. Mech. **20**, 241 (1940).
[2] T. v. Kármán, Z. Angew. Math. Mech. **1**, 233 (1921).
[3] G. Batchelor, Q. J. Mech. Appl. Math. **4**, 29 (1951).
[4] H. Greenspan, *The Theory of Rotating Fluids* (Cambridge University Press, Cambridge, 1968).
[5] O. Savaş, Phys. Fluids **26**, 3445 (1983).
[6] O. Savaş, J. Fluid Mech. **183**, 77 (1987).
[7] J. Lopez and P. Weidman, J. Fluid Mech. **326**, 373 (1996).
[8] G. Gauthier, P. Gondert, and M. Rabaud, J. Fluid Mech. **386**, 105 (1999).
[9] R. Lingwood, J. Fluid Mech. **331**, 405 (1997).
[10] H. Schlichting, *Boundary Layer Theory* (McGraw-Hill, New York, 1987).
[11] F. Bertolotti, T. Herbert, and P. Spalart, J. Fluid Mech. **242**, 441 (1992).
[12] M. Khorrami, Int. J. Numer. Methods Fluids **12**, 825 (1991).
[13] T. Bridges and P. Morris, J. Comput. Phys. **55**, 437 (1984).